

Implications of the $z > 5$ Lyman- α forest for the 21-cm power spectrum from the epoch of reionization

Janakee Raste^{1*}, Girish Kulkarni¹, Laura C. Keating², Martin G. Haehnelt^{3,4},
Jonathan Chardin⁵, Dominique Aubert⁵

¹Tata Institute of Fundamental Research, Homi Bhabha Road, Mumbai 400005, India

²Leibniz Institute for Astrophysics Potsdam (AIP), An der Sternwarte 16, D-14482 Potsdam, Germany

³Institute of Astronomy, University of Cambridge, Madingley Road, Cambridge CB3 0HA, UK

⁴Kavli Institute of Cosmology, University of Cambridge, Madingley Road, Cambridge CB3 0HA, UK

⁵Observatoire Astronomique de Strasbourg, 11 rue de l'Université, 67000 Strasbourg, France

Accepted —. Received —; in original form —

ABSTRACT

Our understanding of the intergalactic medium at redshifts $z = 5\text{--}6$ has improved considerably in the last few years due to the discovery of quasars with $z > 6$ that enable Lyman- α forest studies at these redshifts. A realisation from this has been that hydrogen reionization could end much later than previously thought, so that large “islands” of cold, neutral hydrogen could exist in the IGM at redshifts $z = 5\text{--}6$. By using radiative transfer simulations of the IGM, we consider the implications of the presence of these neutral hydrogen islands for the 21-cm power spectrum signal and its potential detection by experiments such as HERA, SKA, LOFAR, and MWA. In contrast with previous models of the 21-cm signal, we find that thanks to the late end of reionization the 21-cm power in our simulation continues to be as high as $\Delta_{21}^2 = 10 \text{ mK}^2$ at $k \sim 0.1 \text{ h/cMpc}$ at $z = 5\text{--}6$. This value of the power spectrum is several orders of magnitude higher than that in conventional models considered in the literature for these redshifts. Such high values of the 21-cm power spectrum should be detectable by HERA and SKA1-LOW in ~ 1000 hours, assuming optimistic foreground subtraction. This redshift range is also attractive due to relatively low sky temperature and potentially greater abundance of multiwavelength data.

Key words: cosmology: theory – dark ages, reionization, first stars – intergalactic medium

1 INTRODUCTION

Detecting the fluctuating 21-cm signal from neutral hydrogen during the epoch of reionization is a major goal of extragalactic astronomy in the coming decade. Several experiments have published upper limits on this signal (Paciga et al. 2013; Dillon et al. 2014, 2015; Beardsley et al. 2016; Paul et al. 2016; Patil et al. 2017; Barry et al. 2019; Li et al. 2019; Kolopanis et al. 2019; Trott et al. 2020; Mertens et al. 2020; Patwa et al. 2021) and some other experiments are under development (DeBoer et al. 2017; Ahn et al. 2015; Koopmans et al. 2015). These upper limits have already been used to put constraints on the temperature and ionization state of the IGM (Ghara et al. 2020, 2021).

Most of these ongoing 21-cm experiments work under the assumption that the 21-cm signal peaks when the universe is reionized at the 50% level and that the process of

reionization itself ends at around redshifts of $z \sim 6$, a number conventionally assumed due to early constraints from the Lyman- α and Cosmic Microwave Background (CMB) data. For example, the HERA EOR band is designed to operate at frequencies 100–200 MHz which corresponds to redshifts 6.1 to 13.2. While it is acknowledged that the 21-cm signal has a large uncertainty (Cohen et al. 2017), this heuristic understanding is used to set upper limits on the operating frequencies of the radio experiments.

In recent years, however, large spatial fluctuations observed in the Lyman- α forest at $z \approx 5.5$ have changed our understanding of the end of the epoch of reionization (Fan et al. 2006; Becker et al. 2015; Bosman et al. 2018; Eilers et al. 2018; Becker et al. 2018). The large scatter in the effective optical depth τ_{eff} of the Lyman- α forest at high redshift cannot be explained due to only density or temperature fluctuations in a post-reionization universe (D’Aloisio et al. 2015). It was also found that the large Lyman- α absorption troughs observed by Becker et al.

* E-mail: janakee@theory.tifr.res.in

(2015) and the rapid evolution of τ_{eff} at redshifts 5–6 is difficult to explain using fluctuations in the mean free path of ionizing photons due to spatial variation in the photoionization rate (Davies & Furlanetto 2016). It was proposed that ultraviolet background fluctuations due to rare bright sources such as quasars can explain the large fluctuations in Lyman- α forest τ_{eff} (Chardin et al. 2015, 2017), but the abundance of QSOs at high redshifts is probably too low (Kulkarni et al. 2019b).

Using radiative transfer simulations, Kulkarni et al. (2019a) suggested that the observed large spatial scatter in the Lyman- α forest opacity can arise due to large regions, with sizes of about 100 comoving Mpc, of neutral hydrogen during the last stages of reionization (Keating et al. 2020a). Due to these “neutral islands”, which persist in the low-density regions of the Universe upto $z \approx 5.5$, the end of the reionization is delayed to $z \sim 5.3$ (Nasir & D’Aloisio 2020; Choudhury et al. 2021; Qin et al. 2021). This late reionization model is able to reproduce the distribution of τ_{eff} of the Lyman- β forests at $4 < z < 6$ (Keating et al. 2020b). This model is also consistent with other data, such as the underdensity of Lyman- α emitters (LAEs; Becker et al. 2018) and Lyman-Break Galaxies (LBGs; Kashino et al. 2020) in the vicinity of long Lyman- α absorption troughs (Keating et al. 2020a), the luminosity and angular correlation functions of LAEs (Weinberger et al. 2019), measurements of the Thomson scattering optical depth to the last scattering surface (Kulkarni et al. 2019a), and constraints on the ionized hydrogen fraction from quasar damping wings (McGreer et al. 2015; Greig et al. 2017; Mason et al. 2018; Davies et al. 2018; Greig et al. 2019; Wang et al. 2020).

A delayed reionization history would be consequential for 21-cm experiments as it would shift the target 21-cm signal to higher frequencies. In this paper, we discuss the implications of a late end to the epoch of reionization and a persistence of neutral hydrogen islands at $z < 6$ for the 21-cm power spectrum. We use the radiative transfer simulation presented by Kulkarni et al. (2019a), examine the power spectrum of the 21-cm signal at $z < 6$ and the prospects of detecting it.

We assume a flat Λ CDM universe with $\Omega_b = 0.0482$, $\Omega_m = 0.308$, $\Omega_\Lambda = 0.692$, $h = 0.678$, $n_s = 0.961$, $\sigma_8 = 0.829$, and $Y_{\text{He}} = 0.24$ (Planck Collaboration XVI 2014). The units ‘ckpc’ and ‘cMpc’ refer to comoving kpc and comoving Mpc, respectively. In Section 2, we give details of our simulation and our model of the 21-cm signal. Section 3 presents the 21-cm power spectrum in our model at various redshifts. In Section 4, we discuss the prospects of detecting this signal with four current and upcoming interferometric experiments (MWA, LOFAR, HERA and SKA1-LOW). We end with a discussion in Section 5.

2 METHODOLOGY

2.1 21-cm Signal

In the high-redshift universe, neutral hydrogen (H I) is the most abundant element. The hyperfine transition of the H I ground state corresponds to a photon of frequency $\nu_{21} = 1420.406$ MHz (which corresponds to wavelength $\lambda_{21} = 21.1$ cm). The distortion in the CMB spectrum due to this

transition contains information about the density, temperature and ionization of the H I gas (Madau et al. 1997; Shaver et al. 1999; Gnedin & Shaver 2004; Sethi 2005). This distortion is a function of the ratio of the number of atoms in the two hyperfine states, $n_1/n_0 = (g_1/g_0) \exp(-h_p \nu_{21}/k_B T_S)$, where n_0 (n_1) and $g_0 = 1$ ($g_1 = 3$) are the number density and the degeneracy of atoms in the singlet (triplet) hyperfine state, and h_p is the Planck constant. Note that the spin temperature T_S is the thermal temperature the H I gas would have if the number densities of singlet and triplet states were in thermal equilibrium. The spin temperature is determined by the detailed balance between various processes that can alter the level population of the H I hyperfine states (Field 1958; Pritchard & Loeb 2012), and is given by

$$T_S^{-1} = \frac{T_\gamma^{-1} + x_\alpha T_\alpha^{-1} + x_c T_K^{-1}}{1 + x_\alpha + x_c}. \quad (1)$$

The collision coefficient, x_c , is proportional to the number densities of electrons n_e and neutral hydrogen atoms n_{HI} , and increases with the kinetic temperature T_K . The Lyman- α coupling coefficient x_α is proportional to the number density of Lyman- α photons. Such photons are produced in sources within the galaxies as well as by the interaction of X-ray photons with the IGM (Venkatesan et al. 2001). Repeated scattering of these Lyman- α photons by H I gas at kinetic temperature T_K causes the photon colour temperature T_α to relax to T_K through the Wouthuysen-Field effect (Wouthuysen 1952; Field 1958). Therefore, if $x_{\text{tot}} = x_c + x_\alpha \gtrsim 1$, then T_S is strongly coupled to T_K .

When the background CMB radiation passes through a cloud of H I with spin temperature T_S , 21-cm photons are absorbed from the blackbody spectrum if $T_S < T_{\text{CMB}}$ or emitted into it if $T_S > T_{\text{CMB}}$. The observed change in CMB brightness temperature caused by a cloud at redshift z is,

$$\Delta T_b(\nu_o) = \frac{T_S(z) - T_{\text{CMB}}(z)}{1+z} (1 - e^{-\tau}), \quad (2)$$

where $\nu_o = \nu_{21}/(1+z)$ is the observed frequency, $\tau = \int \alpha_\nu ds$ is the 21-cm optical depth of the cloud, and α_ν is the absorption coefficient. Since the natural broadening of the 21-cm line is very small, its resonance line width is the Doppler width dominated by the motion of the atoms,

$$d\nu = \nu \frac{dv}{c} = \nu \frac{ds}{c} \left[H(z) + \frac{dv_p}{ds} \right]. \quad (3)$$

Here, v_p is the component of the peculiar velocity of the gas parallel to our line of sight and s is the light-travel distance. In our simulation, the comoving size of each cell is $dr = 160/2048$ cMpc/ h (see section 2.2) and the light-travel distance between two cells is $ds \simeq dr/(1+z)$. We can safely assume that there is no significant evolution of cosmological quantities over this distance. Therefore, assuming a top-hat H I line profile function ($\phi(\nu) \simeq 1/\Delta\nu$), the optical depth is

$$\tau = \alpha_\nu \Delta s \propto \frac{c}{\nu} \left[H(z) + \frac{dv_p}{ds} \right]^{-1}. \quad (4)$$

During the matter-dominated epoch, the optical depth is

then

$$\begin{aligned} \tau &\simeq \frac{3^2}{2^8 \pi^2} \frac{A_{21} h_p c^3}{G m_p k_B \nu^2} \frac{H_0}{h} \frac{x_{\text{HI}}(1+\delta)(1+z)^{3/2}}{T_{\text{S}}(1+1/H(z)(dv_p/ds))} \frac{Y_{\text{H}} \Omega_b h^2}{(\Omega_m h^2)^{1/2}} \\ &\simeq x_{\text{HI}}(1+\delta) \left(\frac{8.55 \text{ mK}}{T_{\text{S}}} \right) \left(1 + \frac{1}{H(z)} \frac{dv_p}{ds} \right)^{-1} (1+z)^{3/2} \\ &\quad \times \left(\frac{Y_{\text{H}}}{0.76} \right) \left(\frac{\Omega_b h^2}{0.022} \right) \left(\frac{0.14}{\Omega_m h^2} \right)^{1/2}. \end{aligned} \quad (5)$$

When the peculiar velocity gradient is negligible compared to the Hubble flow ($|dv_p/ds| \ll H(z)$), this optical depth is small ($\tau \ll 1$), and we can approximate $(1 - e^{-\tau}) \simeq \tau$ in Equation (2). In our simulation, most grid cells satisfy the condition $|dv_p/ds| \ll H(z)$. For the small number of cells with larger peculiar velocity gradient, we apply a cutoff on the peculiar velocity gradient $|dv_p/ds| \leq 0.5H(z)$ following previous literature (Santos et al. 2010; Mesinger et al. 2011; Mao et al. 2012). As our focus in this paper is on the end of reionization, at lower redshifts, we expect the effect of redshift space distortions to be small (Jensen et al. 2013; Majumdar et al. 2014).

Finally, the differential brightness temperature is,

$$\begin{aligned} \Delta T_b(\nu_o) &\simeq \tau \frac{T_{\text{S}}(z) - T_{\text{CMB}}(z)}{1+z} \\ &\simeq 27 \text{ mK } x_{\text{HI}}(1+\delta) \left(1 - \frac{T_{\text{CMB}}(z)}{T_{\text{S}}} \right) \\ &\quad \times \left(1 + \frac{1}{H(z)} \frac{dv_p}{ds} \right)^{-1} \left(\frac{1+z}{10} \right)^{1/2} \\ &\quad \times \left(\frac{Y_{\text{H}}}{0.76} \right) \left(\frac{0.14}{\Omega_m h^2} \right)^{1/2} \left(\frac{\Omega_b h^2}{0.022} \right). \end{aligned} \quad (6)$$

Here, ΔT_b is a function of both the redshift of observation (through ν_o) and the direction of observation. Fluctuations in HI density (δ), ionization state (x_{HI}), spin temperature (T_{S}) and peculiar velocity gradient (dv_p/ds) contribute to the spatial fluctuations of ΔT_b at any redshift.

In our work, we assume that at $z \leq 10$, (a) the spin temperature is strongly coupled to the kinetic temperature through Lyman- α coupling ($T_{\text{S}} = T_{\text{K}}$), and (b) the gas is sufficiently heated ($T_{\text{K}} \gg T_{\text{CMB}}$). Then Eq. 6 can be simplified as,

$$\begin{aligned} \Delta T_b(\nu_o) &\simeq 27 \text{ mK } x_{\text{HI}}(1+\delta) \left(1 + \frac{1}{H(z)} \frac{dv_p}{ds} \right)^{-1} \\ &\quad \times \left(\frac{1+z}{10} \right)^{1/2} \left(\frac{Y_{\text{H}}}{0.76} \right) \left(\frac{0.14}{\Omega_m h^2} \right)^{1/2} \left(\frac{\Omega_b h^2}{0.022} \right). \end{aligned} \quad (7)$$

In this case, the global 21-cm signal is always in emission ($\langle \Delta T_b \rangle > 0$) and small ($\langle \Delta T_b \rangle < 28 \text{ mK}$ at $z < 10$). The only sources of fluctuations are density, ionization and line-of-sight peculiar velocity gradient. The assumption $T_{\text{K}} \gg T_{\text{CMB}}$ is a plausible approximation at redshifts of our interest, since heating due to X-rays from first sources is expected to raise temperature of the neutral gas well above the T_{CMB} by $z \sim 10$ (Bowman et al. 2018; Ghara et al. 2021). Some recent models have suggested that X-ray heating might be delayed to $z < 10$ (Fialkov et al. 2014; Madau & Fragos 2017; Mirocha et al. 2017; Cohen et al. 2017; Park et al. 2020; Mebane et al. 2020). Our assumption ($T_{\text{S}} \gg T_{\text{CMB}}$) will not be valid in such scenarios, but other than the redshift of heating transition ($T_{\text{K}} \simeq T_{\text{CMB}}$), the spin temperature fluctuations are only expected to enhance the power spectrum

of 21-cm signal (Fialkov et al. 2014; Mesinger et al. 2014; Raste & Sethi 2018, 2019; Ma et al. 2021).

2.2 Simulation

Our fiducial reionization model is that presented by Kulkarni et al. (2019a). We give the essential details here for completeness. The simulation is performed in two stages. In the first stage, a cosmological hydrodynamical simulation is performed in order to obtain the gas density and velocity fields. In the second stage, the radiative transfer is computed to obtain the distribution of the neutral hydrogen during the epoch of reionization. We used the P-GADGET-3 code, a modified version of the GADGET-2 code (Springel et al. 2001; Springel 2005), for the hydrodynamic simulation. Our box size is $160 h^{-1} \text{ cMpc}$, with periodic boundary conditions, and there are 2048^3 gas and dark matter particles. The simulation is evolved from $z = 99$ down to $z = 4$. Snapshots of gas density, halo masses, and other quantities are saved at 40 Myr intervals. This hydrodynamical simulation is similar to the simulations from the Sherwood Simulation Suite (Bolton et al. 2017). Our initial conditions are identical to the initial conditions used in their 160–2048 simulation.

The mean free path of ionizing photons is set by self-shielded regions with a typical overdensity of $\Delta = 10\text{--}100$ (Pawlik et al. 2009; Chardin et al. 2018). Therefore, it is safe to use the QUICK_LYALPHA option in P-GADGET-3, which simplifies galaxy formation and speeds up the simulation by converting gas particles with temperature less than 10^5 K and overdensities greater than 1000 to star particles (Viel et al. 2004) and removing them from the hydrodynamical calculation.

In order to improve the accuracy of the small-scale hydrodynamics, heat is injected in the simulation box to obtain a realistic pressure smoothing at lower redshifts. To accomplish this, instantaneous reionization is assumed at redshift $z = 15$ and ionization equilibrium with the metagalactic UV background is modelled according to a modified version of Haardt & Madau (2012) reionization model. This yields IGM temperatures that agree with measurements by Becker et al. (2011). The pressure smoothing scale at redshifts $z > 5$ for this UV background is less than $100 h^{-1} \text{ ckpc}$ (Kulkarni et al. 2015; Oñorbe et al. 2017), which is approximately equal to the cell size of our grid ($78.125 h^{-1} \text{ ckpc}$, described below). Therefore, the absence of the coupling between the radiative transfer and the gas hydrodynamics does not significantly affect our computation of Lyman- α opacities from the simulation for calibration.

The radiative transfer is computed using the ATON code (Aubert & Teyssier 2008, 2010). We grid the gas density by projecting the smooth particle hydrodynamic (SPH) kernel in our simulation onto a Cartesian grid. The number of grid cells is set to be equal to the number of gas particles in the simulation (2048^3). This gives a grid resolution of $78.125 h^{-1} \text{ ckpc}$. Haloes that host our ionization sources are identified using the friends-of-friends algorithm. At $z = 7$, this yields a minimum halo mass of $2.3 \times 10^8 h^{-1} M_{\odot}$, which is close to the atomic hydrogen cooling limit, and the maximum halo mass is $3.1 \times 10^{12} h^{-1} M_{\odot}$. We place sources of ionizing radiation at the centres of in haloes with masses greater than $10^9 M_{\odot}$ as the halo mass function below this mass suffers from incompleteness due to limited resolution

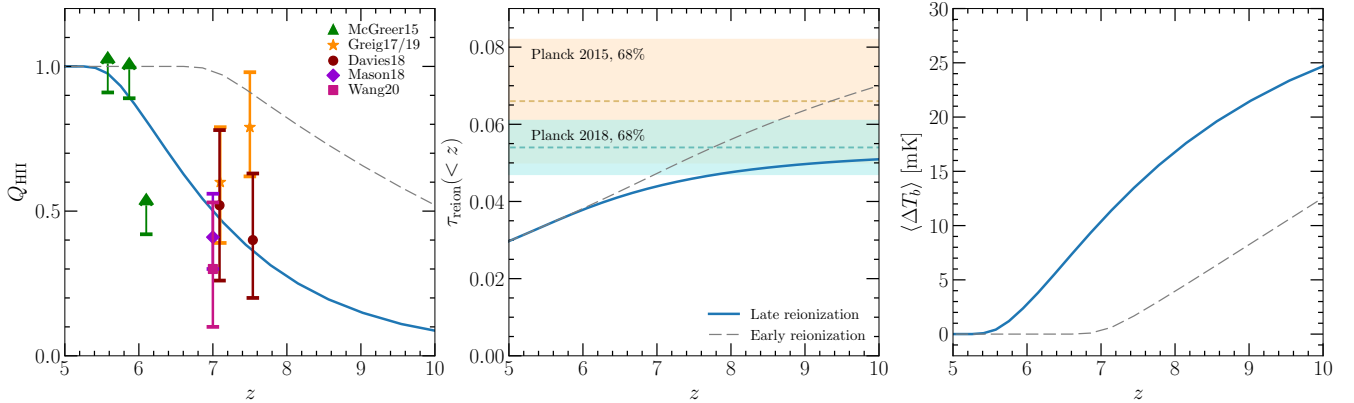


Figure 1. Evolution of the ionized-hydrogen volume fraction Q_{HII} (left panel), cumulative CMB Thomson scattering optical depth τ_{reion} (middle panel) and the global average of the 21-cm differential brightness temperature $\langle \Delta T_b \rangle$ (right panel) in our fiducial simulation (blue curves). Reionization is completed by $z \sim 5.3$ in our model. For comparison we show an early reionization model as the grey dashed curves. We have overlaid constraints on the ionization fraction from Lyman- α absorption studies of quasar spectra (McGreer et al. 2015; Greig et al. 2017; Mason et al. 2018; Davies et al. 2018; Greig et al. 2019; Wang et al. 2020). The middle panel shows τ_{reion} measurements from Planck Collaboration (2016) and Planck Collaboration (2020). The right panel assumes $T_{\text{S}} \gg T_{\text{CMB}}$.

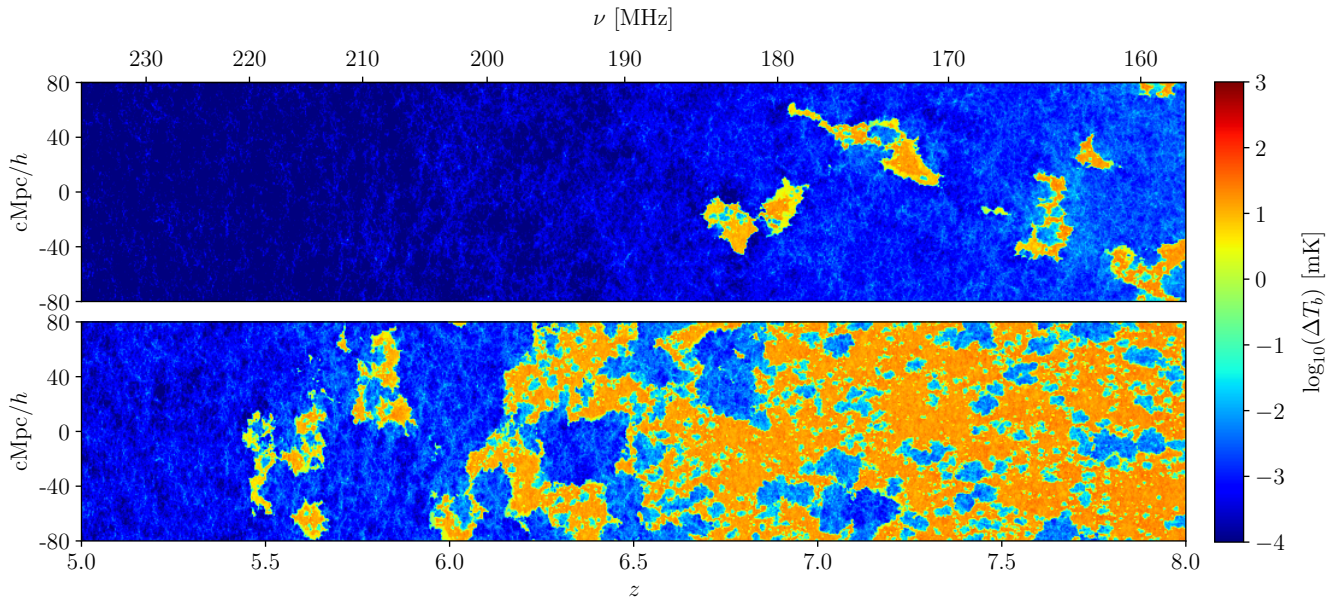


Figure 2. Brightness temperature (ΔT_b) lightcones of early (top panel) and late (bottom panel) reionization models from redshift 8 to 5. In the early model, reionization is completed by $z \sim 6.7$ and the IGM is highly ionized by redshift 5.5. In the late reionization model that is preferred by the $z > 5$ Ly α data, there are large neutral regions present in the IGM at this redshift, which produce a large 21-cm power spectrum signal.

of the simulation. ATON solves the radiative transfer equation by using the M1 approximation (Aubert & Teyssier 2008; Levermore 1984; González et al. 2008) for the first moment. A halo with mass M is assumed to emit hydrogen-ionizing photons with a rate $\dot{N} = \alpha M$ and the average ionizing photon emissivity of the total simulated volume is $\dot{n} = \alpha \sum M/V_{\text{box}}$, where $V_{\text{box}} = L^3 = 160^3$ (cMpc/h) 3 is the simulation box volume and the sum is over all haloes which host sources. The parameter α is the only quantity that is varied in order to calibrate the simulation to given observations, such as the Lyman- α forest (Kulkarni et al. 2019a). It is assumed to be a function of redshift, but in-

dependent of halo mass and it encodes the details of the astrophysical processes such as star formation and photon escape through the inter-stellar medium which govern the ionizing photon production in galaxies. Our assumed scaling between the ionizing luminosity and the halo mass is related to a scaling relation between the observed UV luminosity of high-redshift sources and the halo mass via the unknown ionizing escape fraction. For a mass-independent escape fraction, as a result, we have $L_{\text{UV}} \propto M$. This yields a reasonably good fit to the observed high-redshift galaxy luminosity functions (Chardin et al. 2015), although an even better fit may be obtained if the scaling between L_{UV} and M

is made slightly steeper at low halo masses ($M \lesssim 10^{11} M_\odot$) and flatter at higher halo masses (Trenti et al. 2010). But, as the escape fraction is expected to decrease with halo mass (Kimm et al. 2017), this modified scaling can easily be absorbed in the halo-mass dependence of the escape fraction to yield consistency between our assumed ionizing emissivity and the observed UV luminosity function. All sources are assigned a blackbody spectrum with $T = 70\,000$ K (Keating et al. 2018), which corresponds to an average photon energy of 23.83 eV in the optically-thick limit. A single photon frequency is used for the radiative transfer in order to reduce computational cost. The reionization history is not significantly affected by choice of these parameters, because the simulation is calibrated to match with the Lyman- α forest data. Therefore, any change in the gas temperature due to changing the source spectrum can then be compensated by changing α in the source emissivity above. Finally, we use Equation 7 to calculate differential brightness temperature (ΔT_b) box using the density, ionization, and peculiar velocity boxes. We arbitrarily take the z -axis of the simulation box as the line-of-sight direction and calculate the peculiar velocity gradient along this axis. If the peculiar velocity gradient for any cell $dv_p/ds < -0.5H(z)$ ($dv_p/ds > 0.5H(z)$), then we set its value to $-0.5H(z)$ ($0.5H(z)$) (Santos et al. 2010; Mesinger et al. 2011).

In this work we also consider a second radiative transfer simulation in which the evolution of the volume-averaged ionized hydrogen fraction is calibrated to match its evolution in the Haardt & Madau (2012) model of reionization. In this model, reionization is complete at $z \sim 6.7$. The calibration is achieved by adjusting the source emissivity in the simulation at each time step to get the desired ionized fraction evolution. The two simulations are identical in all aspects apart from the source emissivity. In this paper, we refer to the Haardt & Madau (2012) model of reionization as ‘early reionization model’, while referring to our fiducial simulation (Kulkarni et al. 2019a) as the ‘late reionization model’.

3 RESULTS

We show the ionization history of our model in Figure 1. As discussed by Kulkarni et al. (2019a), the presence of self-shielded neutral hydrogen islands at low redshift delays the end of reionization, which is completed by $z \sim 5.3$. We compare our results with the early reionization model of Haardt & Madau (2012). In this model, the volume averaged ionization fraction reaches 0.5 at $z \sim 10$ and the reionization ends at $z \sim 6.7$. In our late reionization model, the mid-point of reionization is delayed to $z \sim 7$; this is in agreement with the inference from Lyman- α absorption studies of quasar spectra at $5 < z < 8$ (McGreer et al. 2015; Greig et al. 2017; Mason et al. 2018; Davies et al. 2018; Greig et al. 2019; Wang et al. 2020).

In the middle panel of Figure 1, we show the Thomson scattering optical depth, $\tau_{\text{reion}} = 0.054 \pm 0.007$, by Planck Collaboration (2020) as a blue shaded region. Previous measurements of τ_{reion} predicted an earlier epoch of reionization. For example, the orange shaded region in the figure corresponds to the $\tau_{\text{reion}} = 0.066 \pm 0.016$, given by Planck Collaboration (2016). The integrated Thomson scattering

optical depth of the reionization history of our late reionization model is compatible with the latest measurement of τ_{reion} . The early reionization model predicts a higher τ_{reion} , which disagrees with Planck Collaboration (2020), but was consistent with earlier measurements of τ_{reion} .

Figure 1 also shows the evolution of the globally averaged 21-cm signal in our simulations. As discussed in the previous section, we assume that the H I spin temperature $T_s \gg T_{\text{CMB}}$ at $z \leq 10$. As a result, our globally averaged 21-cm differential brightness temperature is small and positive ($0 \leq \langle \Delta T_b \rangle \leq 28$) (Equation 7). With the progress of reionization, the brightness temperature decreases. We show the brightness temperature lightcones for these two models in Figure 2 at redshifts 5–8. The blue regions, which correspond to low brightness temperature, are ionized, whereas the orange regions corresponding to large brightness temperature are neutral. The ionized regions have already overlapped by redshift 8 in the early reionization model, and the regions of substantial brightness temperature disappear by redshift 6.7. At lower redshifts, the brightness temperature structure is well below detection level (see discussion in following section). In the late reionization model, the Universe is mostly neutral at $z = 8$. The ionized regions grow at lower redshifts and large regions (~ 100 cMpc) of substantial brightness temperature are still present in the IGM at redshifts as low as 5.5.

We calculate the 1D spherically averaged power spectrum of a statistically isotropic quantity $F(\mathbf{r})$ as,

$$\langle \tilde{F}(\mathbf{k}_1) \tilde{F}(\mathbf{k}_2) \rangle = (2\pi)^2 \delta_D(\mathbf{k}_1 + \mathbf{k}_2) P_F(k), \quad (8)$$

where, $\tilde{F}(\mathbf{k})$ is the Fourier transform of $F(\mathbf{r})$, δ_D is the Dirac delta function and angular brackets denote ensemble averages. Assuming ergodicity, we take a volume average over k -modes in all directions. Figure 3 shows

$$\Delta_F^2(k) = \frac{k^3}{2\pi^2} \frac{\langle \tilde{F}^2(k) \rangle}{V_{\text{box}}} \quad (9)$$

of the ionized hydrogen fraction and the 21-cm brightness temperature at $z = 5.41$ and $z = 7.14$ in our early and late reionization models. Here, $V_{\text{box}} = 160^3$ (cMpc/h) 3 is the volume of the simulation box. In our fiducial late reionization model we see that both the ionization and brightness temperature power spectra drop as we go from $z = 7.14$ to $z = 5.41$. This is because redshift 7.14 is close to the midpoint of reionization ($Q_{\text{HI}} \simeq 0.5$) in our model (Figure 1). A similar drop is also seen in the early reionization model. However, due to the early end of the reionization in this model, both the ionization and brightness power spectra at redshift 5.41 are orders of magnitude smaller than their counterparts in the late reionization model.

Further, we can also notice in Figure 3 that the ionization power spectrum peaks at different scales in the two models at redshifts 7.14 and 5.41. The peak of the ionization power spectrum shifts to smaller k (larger r) with time, corresponding to the growth of ionized regions. In the late reionization model, the peak of the power spectrum at $z = 7.14$ is at $k \sim 0.9$ h/cMpc and shifts to $k \sim 0.6$ h/cMpc at $z = 5.41$. At small k (large r), the ΔT_b power spectra have a shape similar to the ionization power spectra, while at large k (small r), they have a shape similar to the matter density power spectra. The shape and amplitude of our power spectra at the midpoint and end of reionization broadly match

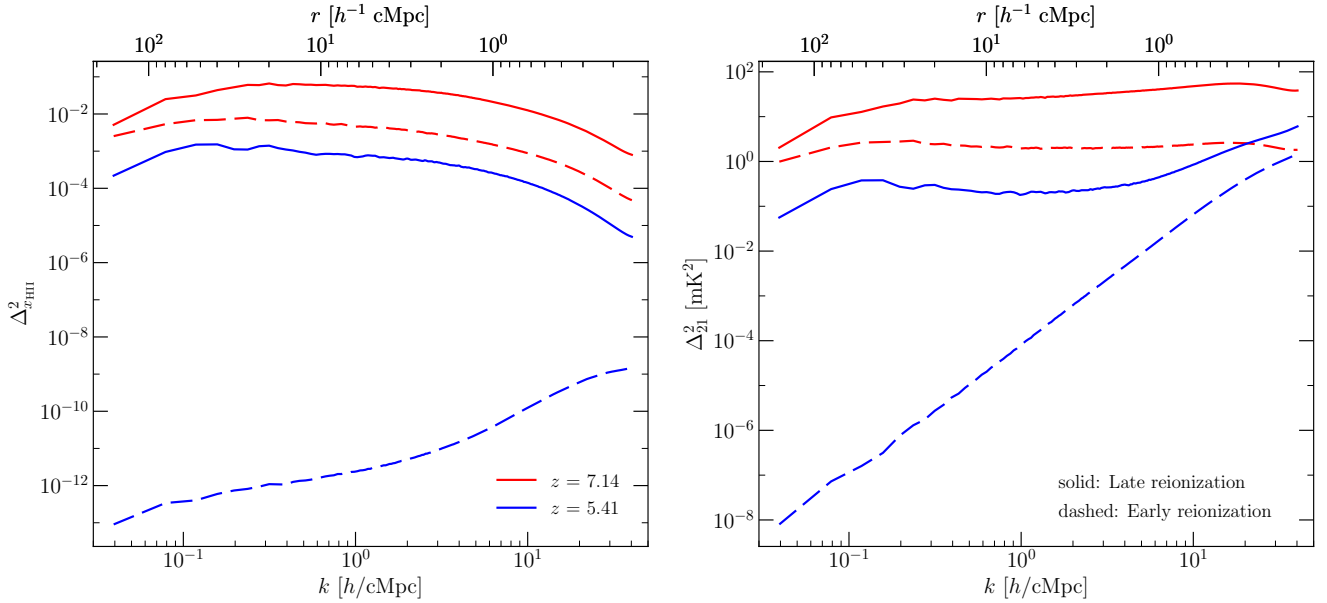


Figure 3. Power spectrum of the ionized-hydrogen fraction (left panel) and the 21-cm brightness temperature (ΔT_b) (right panel) at $z = 5.41$ and $z = 7.14$ in our early and late reionization models. At $z < 6$ the late reionization model, preferred by the Ly α data, shows orders of magnitude greater power than the more conventional early reionization model. In the late reionization model, the ionization power spectrum peaks at $z = 7.14$, which approximately corresponds to the mid-point of reionization (Figure 1). The power spectrum decreases at lower redshifts in this model. We also note that with time the peak of the power spectra shifts to smaller k (larger r) due to the growth of the ionized regions. The brightness temperature fluctuations are due to both the density and ionization fluctuations. On large scale (small k), the ΔT_b fluctuations show a peak at roughly the same scale where ionization fluctuations have a peak. However, at small scales (large k), they have a shape similar to the density fluctuations.

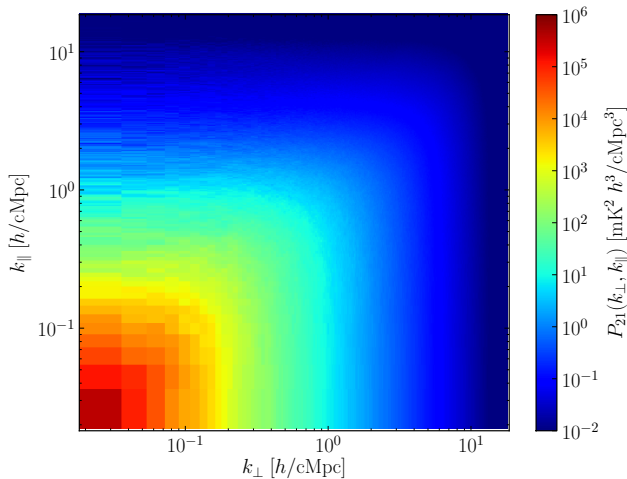


Figure 4. Two-dimensional cylindrically-averaged 21-cm power spectrum at $z = 5.58$ in our model.

with the literature (Zahn et al. 2011; La Plante et al. 2014; Ghara et al. 2015; Hutter 2018; Hutter et al. 2021; Bianco et al. 2021).

Redshift-space distortions caused by the line-of-sight peculiar velocities will introduce anisotropy in the ΔT_b power spectra between k -modes which are parallel (k_{\parallel}) and perpendicular (k_{\perp}) to the line-of-sight. We compute the 2D cylindrical power spectra $P_{21}(k_{\perp}, k_{\parallel}) = \langle \tilde{T}_b^2(k_{\perp}, k_{\parallel}) \rangle / V_{\text{box}}$, where we separately average over the k_{\perp} (along z -axis) and k_{\parallel} (in xy -plane) modes. We show $P_{21}(k_{\perp}, k_{\parallel})$ at $z = 5.58$ in

Figure 4 for our late reionization model. As seen in Figure 3, the ΔT_b fluctuations are dominated by ionization fluctuations when the ionization fraction is large, and the effect of peculiar velocity is small at these redshifts (Jensen et al. 2013; Majumdar et al. 2014).

4 PROSPECTS OF DETECTION

Many ongoing and upcoming radio interferometric experiments are trying to detect the power spectrum of the 21-cm signal. GMRT (Giant Metrewave Radio Telescope; Paciga et al. 2013), LOFAR (Low Frequency Array; Yatawatta et al. 2013; van Haarlem et al. 2013), MWA (Murchison Widefield Array; Tingay et al. 2013; Bowman et al. 2013; Wayth et al. 2018), and PAPER (Donald C. Backer Precision Array for Probing the Epoch of Reionization; Parsons et al. 2010) have published upper limits for power spectrum estimates (see Section 4.3). HERA (Hydrogen Epoch of Reionization Array; DeBoer et al. 2017) has started taking experimental observations while it is still under construction. SKA1-LOW (the low-frequency component of the Square Kilometre Array; Koopmans et al. 2015) is planned to be operational in the next decade.

We use the publicly available code 21CMSENSE¹ (Pober et al. 2013, 2014) to study the possibility of detecting the 21-cm signal with MWA, LOFAR, HERA and SKA1-LOW at various redshifts. Table 1 summarises the relevant observational

¹ 21CMSENSE: <https://github.com/jpober/21cmSense>

Table 1. Summary of observational parameters of four instruments: MWA, LOFAR, HERA and SKA1-LOW. The number of antenna elements are given as core antennas + remote/outtrigger antennas. The effective collecting area A_e is measured at 150 MHz at the zenith. The full-width at half maximum (FWHM), the field of view, and the angular resolution are also given for 150 MHz.

Parameter	MWA ^a [High] [Low]	LOFAR ^b HBA	HERA ^c [EoR]	SKA1-LOW ^d
Number of antennae, N_a	128 + 128	48 + 22	320 + 30	224 + 288
Number of antennae used in 21CMSENSE	128	48	331	224
Core radius r_{core} [m]	300	2000	150	500
Maximum radius, r_{max} [km]	3.5	~ 1000	0.45	40
Minimum baseline, b_{min} [m]	7.7	35	14.6	35.0
Maximum baseline, b_{max} [km]	5.3	1500	0.879	65
Minimum baseline from 21CMSENSE, $b_{\text{min},21}$ [m]	7.72	35.71	14	35.1
Maximum baseline from 21CMSENSE, $b_{\text{max},21}$ [km]	0.741	3.55	0.28	0.887
Element size [m]	4	30.75	14	38
Effective collecting area A_e at 150 MHz [m ²]	21.5	512.0	154	600
FWHM at 150 MHz [deg]	26	3.80	9	3
Field of view at 150 MHz [deg ²]	610	11.35	64	12.5
Angular resolution at 150 MHz	2'	3'	11'	5'
Angular resolution of core ($1.22 \lambda/b_{\text{max},21}$)	11.32'	2.36'	29.96'	9.46'
$k_{\perp,\text{min}}$ at $z = 5.5$ [h/cMpc]	0.006	0.027	0.011	0.027
$k_{\perp,\text{max}}$ at $z = 5.5$ [h/cMpc]	0.566	2.711	0.214	0.677
Minimum frequency, ν_{min} [MHz]	70 [167] [139]	120	50 [100]	50
Maximum frequency, ν_{max} [MHz]	300 [197] [167]	240	250 [200]	350
Maximum redshift, z_{max}	19.29 [7.5] [9.2]	10.83	27.4 [13.2]	27.4
Minimum redshift, z_{min}	3.73 [6.2] [7.5]	4.92	4.7 [6.1]	3.06
Frequency (spectral) resolution [kHz]	40	61	97.8	70
Number of channels (in 8 MHz BW)	200	131	82	114
$k_{\parallel,\text{min}}$ at $z = 5.5$ [h/cMpc]	0.08	0.08	0.08	0.08
$k_{\parallel,\text{max}}$ at $z = 5.5$ [h/cMpc]	8.2	5.38	3.35	4.69
Latitude	26°42'12''S	52°54'32''N	30°43'17''S	26°49'29''S
Longitude	116°40'16''E	6°52'08''E	21°25'42''E	116°45'52''E

^a MWA: Tingay et al. (2013); Wayth et al. (2018); <https://www.mwatelescope.org/telescope>; antenna coordinates from <https://www.mwatelescope.org/telescope/configurations/phase-ii>

^b LOFAR: van Haarlem et al. (2013); <http://www.lofar.org/about-lofar/system/lofar-numbers/lofar-numbers.html>

^c HERA: Dillon & Parsons (2016); DeBoer et al. (2017)

^d SKA1-LOW: de Lera Acedo et al. (2020); antenna coordinates from https://astronomers.skatelescope.org/wp-content/uploads/2016/09/SKA-TEL-SK0-0000422_02_SKA1_LowConfigurationCoordinates-1.pdf

parameters of these instruments. We next discuss these parameters and our choice of antenna configuration for each instrument.

4.1 Interferometric Experiments

The antenna configuration for each instrument consists of a cluster of short-baseline antennas ('core'), surrounded by a few 'outtrigger' or 'remote' antennas. The long baselines corresponding to remote/outtrigger antennas are useful for calibration and foreground removal purposes; however, for sensitivity calculations of EoR fields, only the short baselines are useful. Therefore, in our work we have considered only the core configuration for each antenna array and have ignored the remote/outtrigger antennas. In Table 1, we have listed the total number of antennas N_a as number of antennas in core N_c + remote/outtrigger antennas N_r .

MWA Phase II uses a compact configuration for EoR studies (Phase IIA). The radius for this configuration (r_{core}) is about 300 m and it consists of 128 tiles. Of these, 72 tiles are in two hexagonal cores and 56 tiles are pseudo-randomly distributed (Li et al. 2019). The shortest and longest base-

lines for this configuration are 7.7 m and 741 m respectively, whereas the longest baseline for the complete configuration (compact + extended) is 5.3 km (Wayth et al. 2018). The compact and extended baselines correspond to a resolution (at 150 MHz) of about 11' and 2' respectively. MWA tiles have an approximate side of length 4 m, corresponding to 26° of FWHM at 150 MHz (Jacobs et al. 2016) and a large field of view of about 610 deg² (Tingay et al. 2013).

LOFAR consists of two antenna arrays: the Low Band Antennas (LBA) observe at 10–80 MHz and the High Band Antennas (HBA) observe at 120–240 MHz. We only consider the HBA array, because it covers the redshift range $z = 4.92$ – 10.83 . The 24 HBA core stations are located within a radius of around 2 km (van Haarlem et al. 2013). Further, around 22 remote stations are located within the Netherlands (with baseline up to 100 km) and many international stations (with baseline up to 1500 km) are spread within the Europe. The core HBA stations are used in split mode, therefore their total number is 48, and the shortest and longest baselines are 35 m and 3.5 km respectively. Patil et al. (2017) have discussed that even though the shortest baseline for LOFAR HBA is ~ 35 m, LOFAR HBA EoR studies have discarded the

short baselines (< 127 m) that correspond to pairs of antennas sharing common electronics (Patil et al. 2017; Mertens et al. 2020). Therefore, 100 m is often quoted in the literature as the shortest LOFAR baseline. Long baselines ($> 250 \lambda_o$, where λ_o is the central wavelength of observation) are also discarded for EoR studies. In our work, we have used all baselines corresponding to all 48 core HBA stations. These are the longest baselines amongst all four instruments, giving resolution of $3'$ at 150 MHz. LOFAR HBA core, remote and international stations have different diameters, 30.75 m, 41.05 m and 56.50 m respectively; we only use one element diameter of 30.75 m in our sensitivity calculations, which corresponds to a field of view of 11.35 deg^2 at 150 MHz (van Haarlem et al. 2013).

The ‘split-core configuration’ of HERA is planned to have 350 antenna elements, of which 320 elements will be in a densely packed hexagonal core and 30 elements will be outriggers (DeBoer et al. 2017). The core will be split in 3 sections (hence the name ‘split-core’), offset by non-integer fractions of a hex spacing. A core hexagon of 19 elements (with each side having 3 elements), had started taking observations in 2017 (DeBoer et al. 2017). Two outrigger antennas were added in 2019 to improve foreground imaging (Morgan et al. 2019). However, since the final antenna coordinates are not publicly available yet, in our calculations we assume a perfect hexagon with 331 elements (with each side having 11 elements) (Dillon & Parsons 2016) in our calculations and we have ignored the outrigger antennas. This difference of 11 antennas will not have a significant effect on our sensitivity predictions. The shortest and longest baselines for this perfect hexagon are 14 m and 280 m respectively, whereas including the outrigger antennas, the longest baselines is 879 m. This corresponds to angular resolution (at 150 MHz) of $30'$ (core) and $11'$ (outriggers). Each HERA element consists of a 14 m dish, with a collecting area of 155 m^2 and a field of view of 64 deg^2 .

With 38 m diameter and a collecting area of 600 m^2 , SKA1-LOW will have the largest element size (de Lera Acedo et al. 2020), with a field of view of about 12.5 deg^2 at 150 MHz. The full SKA1-LOW configuration will extend up to a radius of 40 km and the longest baseline will be 65 km ($7.7''$ resolution at 150 MHz). In our calculations we have used 224 core elements spread within a radius of 500 m. The shortest and longest baseline of the core is 35.1 m^2 and 887 m, respectively. This results in an angular resolution of $10'$ at 150 MHz.

MWA is designed to observe in the frequency range of 70–300 MHz, which corresponds to the redshift range of $3.73 \lesssim z \lesssim 19.29$ for $\lambda_0 = 0.21$ m. However, MWA EoR observations are taken in three bands: ultralow band at 75–100 MHz ($13.2 \lesssim z \lesssim 18$), low band at 139–167 MHz ($7.5 \lesssim z \lesssim 9.2$), and high band at 167–197 MHz ($6.2 \lesssim z \lesssim 7.5$) (Jacobs et al. 2016). The spectral (frequency) resolution of MWA is 40 kHz (Li et al. 2019; Trott et al. 2020). This corresponds to 200 channels in a bandwidth of 8 MHz. LOFAR HBA is optimized for the frequency range 120–240 MHz ($4.9 \lesssim z \lesssim 10.8$); however, the EoR observations are usually carried out in three narrower bands (7.9–8.6, 8.6–9.6 and 9.6–10.6) and the fre-

quency resolution is 61 kHz for EoR studies (Patil et al. 2017; Mertens et al. 2020). While the LOFAR observations can have a typical duration of 12–16 hr per day (Mertens et al. 2020), we have only assumed 6 hr of observation duration per day for all instruments. For HERA the extended frequency range is 50–250 MHz ($4.7 < z < 27.4$) and its EoR frequency band is 100–200 MHz ($6.1 < z < 13.2$), with a frequency resolution of 97.8 kHz (DeBoer et al. 2017). SKA1-LOW is planned to work in the frequency range of 50–350 MHz ($3 < z < 27.4$). If this whole frequency band is available for 21-cm observations, then SKA1-LOW will provide us information from the formation of first stars and galaxies to the end of hydrogen reionization. In next subsection we present results for all four instruments in the redshift range $5 < z < 6$, assuming that their observational range extends to these redshifts.

4.2 Sensitivity of 21-cm Observations

In this subsection, we discuss the 21CMSENSE code used to calculate the sensitivity of various observational instruments and present the comparison for 1080 hr of observation (6 hr of tracking mode observation per day, for 180 days). Sensitivity of an instrument indicates how weak a signal can be detected by that instrument. In the absence of the signal, the noise detected by the instrument is a Gaussian random variable with zero mean. Hence, statistically independent observations can be combined to improve upon the sensitivity $\Delta_{N,0}^2(k)$. This improvement is inversely proportional to the square root of the number of samples N_s ($\Delta_N^2(k) = \Delta_{N,0}^2(k)/\sqrt{N_s}$).

Given an antenna configuration for an interferometer and the wavelength of observation $\lambda(z)$, the baseline distribution is calculated by 21CMSENSE using $u_{ij}(z) = b_{ij}/\lambda(z)$, where b_{ij} is the physical distance between a pair of antennas i and j . While it is possible to specify the minimum and maximum baseline length while using 21CMSENSE for sensitivity calculations, we use all the baselines provided by the antenna configuration in our calculations (see discussion above). Given N_a number of antennas, the total number of baselines is $N_a(N_a - 1)/2$. As each baseline is an independent measurement, the number of data samples increases with the number of baselines ($N_s \propto N_a^2$).

The angle extended over the sky by a baseline u is $\theta \simeq 1/u$. This approximation is only valid when the angle θ is small (small angle approximation). The transverse distance in the sky extended by angle θ at redshift z is (Furlanetto et al. 2006),

$$l_{\perp}(z) = X(z)\theta \approx 1.9 \text{ cMpc}/h \left(\frac{1+z}{10} \right)^{0.2} \left(\frac{\theta}{1 \text{ arcmin}} \right). \quad (10)$$

Therefore, k mode of the power spectrum perpendicular to the line-of-sight (k_{\perp}) at redshift z for $u \gg 1$ is $k_{\perp}(z) \simeq 2\pi/l_{\perp}(z) \simeq (2\pi/X(z))u$. The smallest and largest k_{\perp} modes probed at any redshift are determined by the smallest and largest baseline lengths respectively (b_{\min} and b_{\max}). At $z = 5.5$, $X(z) = 1.743 \text{ cMpc}/h/\text{arcmin}$ and $\lambda_o = 1.37$ m. Therefore for a baseline of 10 m, $u_{10\text{m}}(5.5) = 7.28$ and the transverse k -mode probed is, $k_{\perp,10\text{m}}(5.5) \sim 0.0076 \text{ cMpc}/h$. For a 100 m baseline, $k_{\perp,100\text{m}}(5.5) \sim 0.076 \text{ cMpc}/h$.

Ignoring redshift-space distortions, the line of sight distance at redshift z covered by observational frequency range

² Note that this length is *smaller* than the planned tile diameter of 38 m (de Lera Acedo et al. 2020).

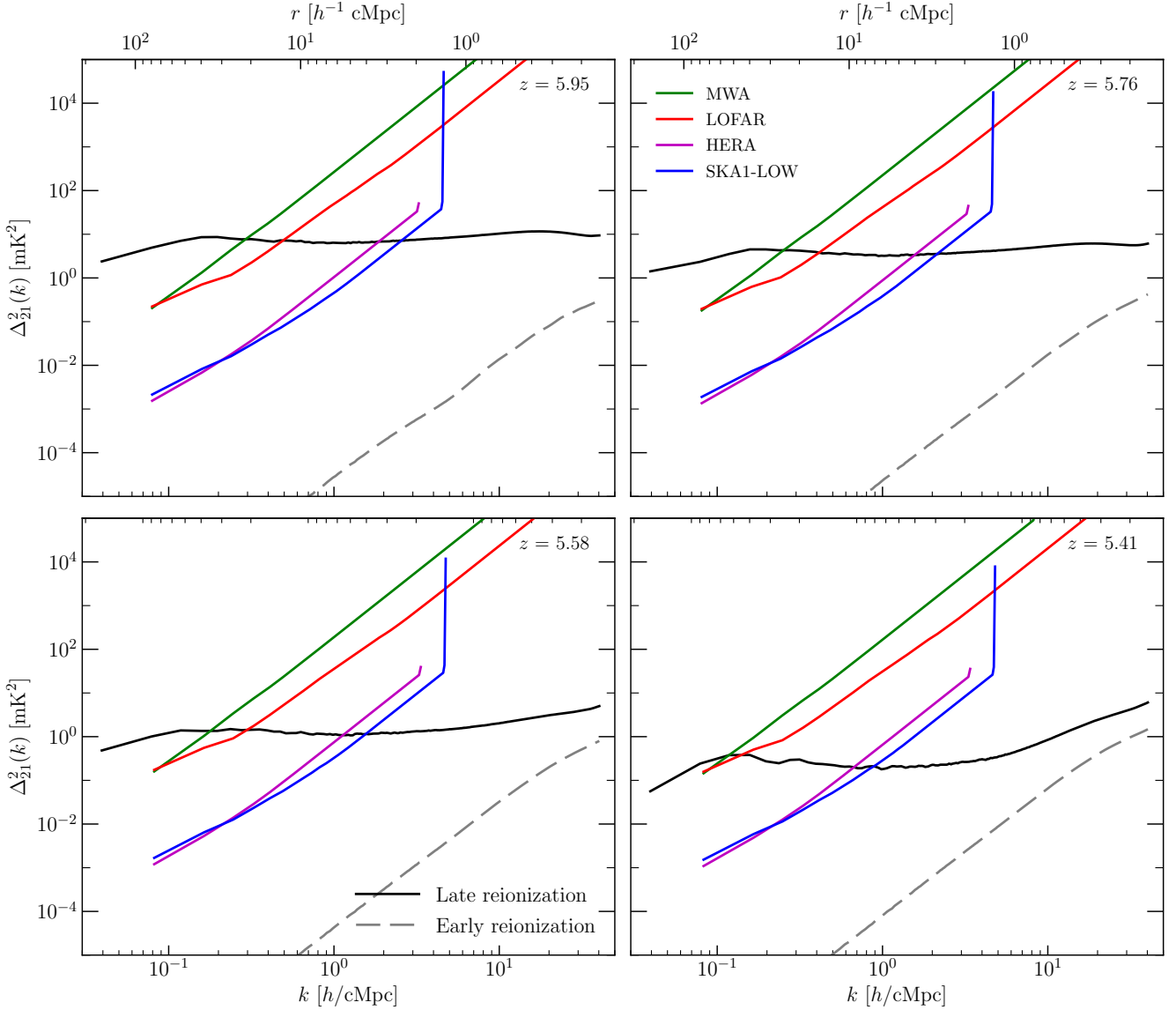


Figure 5. The 21-cm power spectra from our models compared to the noise power spectra for MWA (green curves), LOFAR (red curves), HERA (magenta curves), and SKA1-LOW (blue curves), for tracking mode observations of 6 hours a day, 180 days (total 1080 hours) at $z = 5.94$ ($\nu = 204$ MHz; top left panel), $z = 5.76$ ($\nu = 210$ MHz; top right panel), $z = 5.58$ ($\nu = 216$ MHz; bottom left panel) and $z = 5.41$ ($\nu = 221$ MHz; bottom right panel). Black solid curves correspond to power spectra from our preferred late reionization model. Grey dashed curves show predictions for an early reionization model.

$\Delta\nu$ is (Furlanetto et al. 2006),

$$l_{\parallel}(z) = Y(z)\Delta\nu$$

$$\approx 11.5 \text{ cMpc}/h \left(\frac{1+z}{10} \right)^{0.5} \left(\frac{\Omega_m h^2}{0.15} \right)^{-0.5} \left(\frac{\Delta\nu}{1 \text{ MHz}} \right), \quad (11)$$

and the line of sight k -mode at redshift z is $k_{\parallel}(z) = (2\pi/Y(z))\eta$, where the delay parameter η is the Fourier transform of the frequency range $\Delta\nu$. The smallest and largest k_{\parallel} modes probed are determined by the cosmological bandwidth B and channel width $\Delta\nu_c$ respectively. Here B is the redshift range that can be considered cosmologically co-eval. We have used 8 MHz as default value for the bandwidth in our calculations using 21CMSENSE. The number of samples increases with the bandwidth as $N_s \propto B$.

Therefore, $\Delta_N^2(k) \propto \Delta_{N,0}^2(k)/\sqrt{B}$. The number of channels in the bandwidth ($n_{\text{chan}} = B/\Delta\nu_c$) is a function of the instrument (see Table 1). It affects the maximum k -mode that can be probed, but does not have a significant effect on the sensitivity.

If the total number of days observed is n_{days} and the number of observing hours per day is $t_{\text{per-day}}$, then the sensitivity of the instrument is (Parsons et al. 2012),

$$\Delta_N^2(k) \approx \frac{X^2 Y}{4\pi^2} [k]^{\frac{5}{2}} [\Omega] \left[\frac{1}{t_{\text{per-day}}} \right]^{\frac{1}{2}} \left[\frac{1}{n_{\text{days}}} \right] \left[\frac{1}{B} \right]^{\frac{1}{2}} \left[\frac{1}{\Delta \ln(k)} \right]^{\frac{1}{2}} \left[\frac{1}{N_a} \right] \left[\frac{f_0}{f} \right]^{\frac{1}{2}} T_{\text{sys}}^2(u, v, \eta). \quad (12)$$

Here, Ω is the primary beam field of view. It is assumed to

be a 2D Gaussian for all instruments. f and f_0 are baseline redundancy parameters, which we discuss below. $\Delta \ln(k)$ is the number of k -modes in a logarithmic bin.

We have used the ‘moderate’ model for the foreground wedge, where all k -modes inside the horizon are excluded from the sensitivity calculations and all baselines within a uv -pixel are added coherently. Purely north-south baselines are excluded from the calculations. The system temperature has contributions from both the sky and the instrument ($T_{\text{sys}} = T_{\text{sky}} + T_{\text{rec}}$). We have taken the receiver temperature to be $T_{\text{rec}} = 100$ K for all instruments and the sky temperature is taken to be (Thompson et al. 2001),

$$T_{\text{sky}} = 60 \text{ K} \left(\frac{300 \text{ MHz}}{\nu} \right)^{2.55}. \quad (13)$$

The sky temperature decreases with increasing frequency ν , because it is set by synchrotron foregrounds, which are weaker at higher frequencies. T_{sys} is orders of magnitude larger than the 21-cm signal (Equation 6), therefore the first-generation 21-cm observations are expected to have poor signal to noise ratio ($S/N < 1$). Instruments planning to observe the 21-cm signal have been designed to redundantly sample baselines (Dillon & Parsons 2016). If a single baseline with a t_0 integration time and n_i number of t_0 samples in uv -bin i has f_0 sampling redundancy, then the increased sensitivity for a redundant array is $f \equiv f_0 (\sum_i n_i^2 / \sum_i n_i)$ (Parsons et al. 2012).

21CMSENSE uses a detailed version of Equation 12 to calculate instrument sensitivity for a given configuration. In Figure 5, we show our sensitivity predictions for MWA, LOFAR, HERA and SKA1-LOW for redshifts $5 < z < 6$ for 180 days and 6 hours of tracking mode observation duration per day. The total observing time is $n_{\text{days}} \times t_{\text{per-day}} = 1080$ hours. We have shown our late reionization power spectrum prediction in this range, along with the early reionization power spectra. For our late reionization model, HERA and SKA1-LOW will be able to detect the signal at $5.4 \leq z \leq 6$, in 1080 hr of observation and clear distinction between late and early reionization models can be made in this redshift range. MWA and LOFAR HBA can only detect signal at low k -modes at $z > 5.4$.

The minimum value of the k_{\parallel} and k_{\perp} modes depend on the bandwidth (8 MHz) and the minimum baseline of the instrument, respectively. The maximum value of k_{\parallel} and k_{\perp} modes are determined by channel width and maximum baseline (maximum ‘core’ baseline in our case) of the instrument, respectively. Here, the smaller frequency resolution of MWA and the large baselines of LOFAR lead to extended sensitivity at large k -modes. In comparison, the large frequency resolution and short core baselines of HERA result in much lower cutoff of k modes. As $k_{\perp, \text{max}}$ increases linearly with the maximum baseline length, assuming the full configuration for MWA and SKA1-LOW instead of the ‘core’ antenna configuration would increase $k_{\perp, \text{max}}$ by an order of magnitude (Table 1). For LOFAR, taking into account the international baselines can theoretically lead to probing k_{\perp} of 10^3 h/cMpc. However, large baselines are not very useful for detecting the 21cm signal as the sensitivity decreases rapidly for high k -modes (Equation (12) and Figure 5). Hence, none of the instruments will be able to probe the signal at these scales at redshifts of interest.

Since most of the reionization models used in the past

predict an end of reionization by $z \sim 6$, these interferometric instruments do not plan to observe at redshifts below 6. For example, the high band of MWA only observes $6.2 \leq z \leq 7.5$ and the EoR band of HERA will observe $6.1 \leq z \leq 13.2$. However, if the reionization of H I ends somewhat later, then there is two to four orders of magnitude more power in 21-cm spectra at $z < 6$ than in, e.g., the early reionization model, and extending the observation frequency of HERA and SKA1-LOW to these redshifts will help to make a clear distinction between these models. It is also important to note that while some instruments (e.g., Dillon et al. 2014) plan to observe post-reionization frequencies to measure the ‘null signal’ due to residual foregrounds, these redshifts might still contain strong 21-cm signal, if reionization ends later than $z \sim 6$.

4.3 Current Upper Limits

In Figure 6 we show the power spectrum from the late and early reionization models at $k = 0.079, 0.197$ and 0.512 h/cMpc. The colour scheme represents a range of k -modes from 0.05 to 0.6 h/cMpc. Our simulated late reionization model has significant power up to redshift $z \sim 5.4$. At $z < 6.4$, these power spectra vary mildly with k (see also Figures 3 and 5). At small scales (large k), our power spectra have large power at all redshifts due to the small-scale structures in the IGM. However, at large scales (small k) the power increases with time as the size of ionized regions increases. Power at all scales declines rapidly towards the end of reionization ($z \lesssim 6$); this corresponds to $x_{\text{HII}} \gtrsim 0.8$ in Figure 1. For $k = 0.2$ h/cMpc, the peak of the power spectra seems to coincide with the midpoint of reionization at $z \sim 7.1$, whereas for larger scales, $k = 0.08$ h/cMpc, the peak of the power spectra is delayed to $z \sim 6.5$ when the ionized regions grow due to percolation in this model. For the early reionization model, the power at all scales is comparable and the evolution due to redshift is negligible. Note that we have ignored the fluctuations due to inhomogeneous spin temperature in this paper ($T_{\text{s}} \gg T_{\text{CMB}}$). While the fluctuations due to inhomogeneous Lyman- α coupling and heating are expected to be small at $z < 10$ (Ghara et al. 2015; Cohen et al. 2017), delayed heating due to inefficient X-ray sources or low escape fraction of X-ray photons can enhance the power spectra by up to two orders of magnitude (Fialkov et al. 2014; Mesinger et al. 2014; Raste & Sethi 2018, 2019; Ma et al. 2021). Therefore, other than the redshift of heating transition ($T_{\text{K}} \simeq T_{\text{CMB}}$, when power at large scale decreases), our power spectra represent conservative limits for their respective reionization model. We hope to analyse the effect of inhomogeneous T_{s} on our late reionization model predictions in future work.

While the Ly α -informed models predict strong 21-cm power spectrum signal at relatively lower redshifts, these low redshifts are also potentially more convenient for experiment. We show our sensitivity predictions for MWA, LOFAR, HERA and SKA1-LOW as function of redshift for 1080 hr of observation at $k = 0.1$ h/cMpc as thin dotted purple curves in Figure 6. We see that HERA and SKA1-LOW have sensitivity comparable at this scale and they will be able to detect the 21-cm signal at $5.4 < z < 10$ in about < 1000 hr of observation. LOFAR and MWA have sensitivities that are worse by about two orders of magnitude. They will be able to detect the 21-cm signal at redshifts around the midpoint

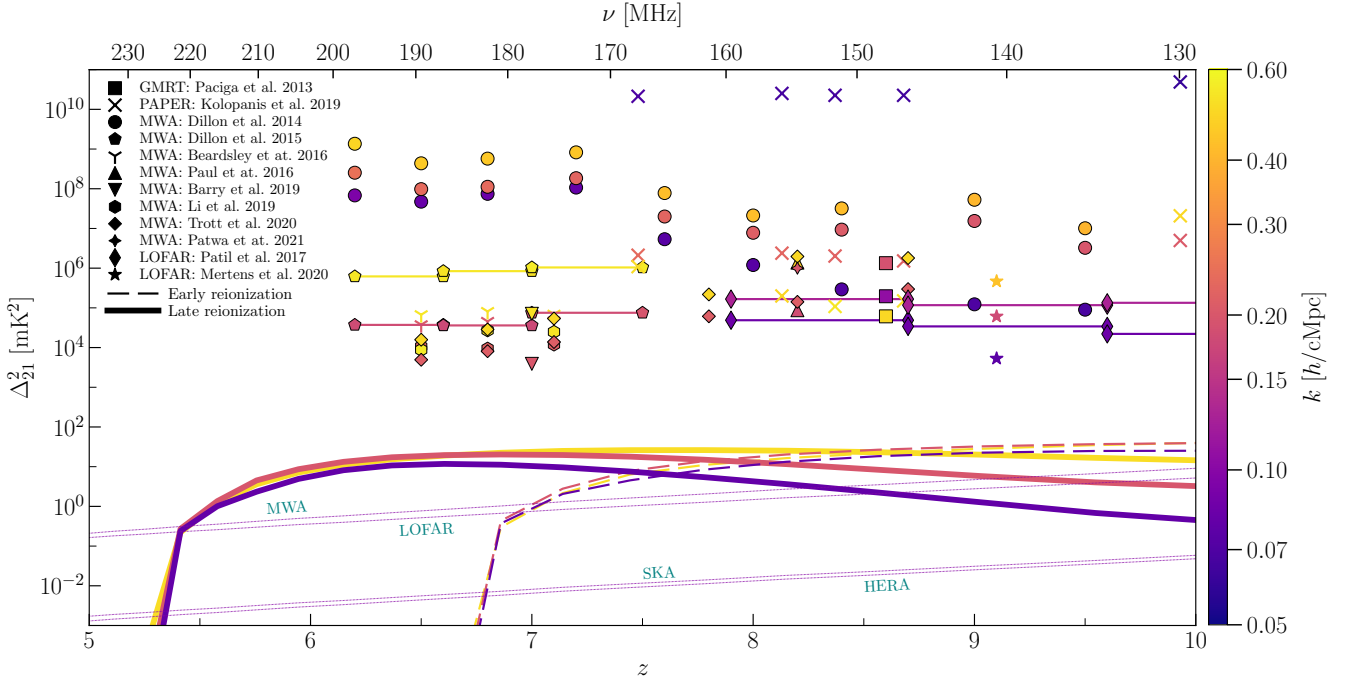


Figure 6. Upper limits on the 21-cm power spectrum Δ_{21}^2 reported by various interferometric experiments compared with the theoretical predictions of the power spectrum values of our simulation at $k = 0.079 h/cMpc$ (yellow solid curve), $k = 0.197 h/cMpc$ (orange solid curve) and $k = 0.512 h/cMpc$ (purple solid curve). The dashed curves show the power spectrum evolution in an early reionization model as discussed in the text. When upper limits are not available at these k values, limits at the closest available k value are shown. The numerical data compilation is presented in Appendix A. Instrument sensitivities of MWA, LOFAR, HERA and SKA1-LOW for 1080 hr of observations at $k = 0.1 h/cMpc$ are shown as dotted purple lines.

of reionization where the 21-cm signal has large power due to fluctuations of the ionization field. All four instrument sensitivities increase at higher redshifts due to increasing sky temperature (Equation 13). For example, the sensitivities increase by an order of magnitude from redshift 5.5 to redshift 8.

So far most 21-cm epoch-of-reionization experiments have focused exclusively at $z > 6$. This is evident in the upper limits on the 21-cm power spectrum reported by these experiments. In Figure 6, we compile several upper limits on the 21-cm power spectrum Δ_{21}^2 . This includes limits published by GMRT (Paciga et al. 2013), LOFAR (Patil et al. 2017; Mertens et al. 2020), MWA (Dillon et al. 2014, 2015; Beardsley et al. 2016; Paul et al. 2016; Barry et al. 2019; Li et al. 2019; Trott et al. 2020; Patwa et al. 2021) and PAPER (Kolopanis et al. 2019) at redshifts $z \leq 10$ at k -modes closest to 0.08, 0.20 and 0.50 $h/cMpc$. Appendix A lists the numerical values of the points in Figure 6. When upper limits are not available at these k values, limits at the closest available k value are shown. All published limits are at $z > 6$. While LOFAR HBA works in the frequency range 120–240 MHz, which corresponds to $4.9 < z < 10.8$, their upper limits for Δ_{21}^2 are given at $7.9 < z < 10.6$ for a wide range of k -modes ($0.053 h/cMpc < k < 0.432 h/cMpc$) (Patil et al. 2017; Mertens et al. 2020). These upper limits from LOFAR at $7.9 < z < 10.6$ are better at smaller k values (large scales). However, at these redshifts the simulated power spectra also decrease rapidly with k . As a result, the upper limits are still about four orders of magnitude higher than the simulation predictions at these redshifts. At $z \sim 8.6$, all four experi-

ments have published upper limits (Paciga et al. 2013; Patil et al. 2017; Kolopanis et al. 2019; Trott et al. 2020), which are currently roughly at the same level. The upper limit provided by Paciga et al. (2013) at $z \sim 8.6$ is less than three orders of magnitude larger than our predicted signal. Upper limits from MWA at $z \sim 8.6$ are also of the similar values (Paul et al. 2016; Trott et al. 2020; Patwa et al. 2021). The minimum redshift studied is $z = 6.5$ by MWA at $0.14 h/cMpc < k < 0.6 h/cMpc$ (Dillon et al. 2015; Beardsley et al. 2016; Li et al. 2019; Trott et al. 2020). They have given the current best limits of Δ_{21}^2 at $6.5 < z < 7.8$. These limits are about two orders of magnitude higher than the predicted signal by our late reionization model. It is interesting to note that the difference between the current upper limits and our model prediction decreases rapidly towards lower redshifts.

5 CONCLUSIONS

Most 21-cm experiments work under the assumption that the epoch of reionization ends at $z \sim 6$. However, radiative transfer simulations that agree with the Ly α data prefer delayed reionization. These models suggest that neutral hydrogen islands of sizes of up to 100 comoving Mpc may persist in the IGM at redshift as low as $z \sim 5.3$. These islands can explain the spatial fluctuations seen in the Lyman- α forest opacity at $z < 6$ (Kulkarni et al. 2019a; Keating et al. 2020a). We show in this paper that due to the presence of these large patches of neutral hydrogen, the power spectrum of 21-cm brightness temperature is significantly enhanced at

redshifts $5 < z < 6$ relative to previous models. We compare the 21-cm power spectra at $z < 6$ with a more conventional reionization model, in which reionization ends at $z > 6$, and find that there is about two to four orders of magnitude difference in the 21-cm power spectra from these two models at these redshifts.

The larger power spectra predicted by our delayed reionization model should be observable at high significance by HERA and SKA1-LOW with observation duration of 180 days with 6 hours per day (total 1080 hours), assuming optimistic foreground subtraction. To achieve a similar sensitivity, MWA and LOFAR will need to observe for about hundred times longer. A prediction of an enhanced 21-cm power spectrum is good news for interferometric experiments as at low redshifts (high frequencies) the thermal noise due to foregrounds is considerably lower ($T_{\text{sky}} \propto \nu_c^{-2.55}$) and the sensitivity of the instruments is correspondingly better. This is worth noting for experimental efforts that have been artificially restricted to $z > 6$. In particular, it might be worthwhile for HERA and SKA1-LOW to plan epoch-of-reionization observations at $z < 6$.

Another benefit of relatively lower redshifts is better synergies with multi-wavelength experiments. Over the next few years, optical/IR facilities such as the James Webb Space Telescope (*JWST*), the Vera C. Rubin Observatory, the Nancy Grace Roman Space Telescope, and Euclid space telescope, in addition to ALMA and the thirty-metre-class telescopes, will provide data at $z \sim 6$ that will potentially identify sources of reionization. The Ly α emitter clustering and luminosity function measurements from facilities such as Subaru/HSC and Subaru/PFS are also available at $z < 7.5$ (Weinberger et al. 2020, 2019). Metal-line intensity mapping experiments such as CONCERTO (Concerto Collaboration 2020) and CCAT-P (Cothard et al. 2020) will also potentially detect the large-scale structure at these redshifts. Cross-correlating 21-cm measurements with these multi-wavelength data sets can potentially yield important scientific insight by reducing parameter degeneracies (Dumitru et al. 2019).

ACKNOWLEDGEMENTS

We thank Somnath Bharadwaj, Tirthankar Roy Choudhury, Avinash Deshpande, Léon Koopmans, Akash Kumar Patwa, and Saurabh Singh for useful comments. This work was supported by a grant from the Swiss National Supercomputing Centre (CSCS) under project ID s949. GK gratefully acknowledges support by the Max Planck Society via a partner group grant. This work used the Cambridge Service for Data Driven Discovery (CSD3) operated by the University of Cambridge (www.csd3.cam.ac.uk), provided by Dell EMC and Intel using Tier-2 funding from the Engineering and Physical Sciences Research Council (capital grant EP/P020259/1), and DiRAC funding from the Science and Technology Facilities Council (www.dirac.ac.uk). This work further used the COSMA Data Centric system operated Durham University on behalf of the STFC DiRAC HPC Facility. This equipment was funded by a BIS National E-infrastructure capital grant ST/K00042X/1, DiRAC Operations grant ST/K003267/1 and Durham University. DiRAC is part of the UK's National E-Infrastructure.

DATA AVAILABILITY

No new data were generated or analysed in support of this research.

REFERENCES

- Ahn K., Mesinger A., Alvarez M. A., Chen X., 2015, *Advancing Astrophysics with the Square Kilometre Array (AASKA14)*, p. 3
- Aubert D., Teyssier R., 2008, *MNRAS*, **387**, 295
- Aubert D., Teyssier R., 2010, *ApJ*, **724**, 244
- Barry N., et al., 2019, *ApJ*, **884**, 1
- Beardsley A. P., et al., 2016, *ApJ*, **833**, 102
- Becker G. D., Bolton J. S., Haehnelt M. G., Sargent W. L. W., 2011, *MNRAS*, **410**, 1096
- Becker G. D., Bolton J. S., Madau P., Pettini M., Ryan-Weber E. V., Venemans B. P., 2015, *MNRAS*, **447**, 3402
- Becker G. D., Davies F. B., Furlanetto S. R., Malkan M. A., Boera E., Douglass C., 2018, *ApJ*, **863**, 92
- Bianco M., Iliev I. T., Ahn K., Giri S. K., Mao Y., Park H., Shapiro P. R., 2021, *MNRAS*, **504**, 2443
- Bolton J. S., Puchwein E., Sijacki D., Haehnelt M. G., Kim T.-S., Meiksin A., Regan J. A., Viel M., 2017, *Mon. Not. Roy. Astron. Soc.*, **464**, 897
- Bosman S. E. I., Fan X., Jiang L., Reed S., Matsuoka Y., Becker G., Haehnelt M., 2018, *MNRAS*, **479**, 1055
- Bowman J. D., et al., 2013, *Publ. Astron. Soc. Australia*, **30**, e031
- Bowman J. D., Rogers A. E. E., Monsalve R. A., Mozdzen T. J., Mahesh N., 2018, *Nature*, **555**, 67
- Chardin J., Haehnelt M. G., Aubert D., Puchwein E., 2015, *MNRAS*, **453**, 2943
- Chardin J., Puchwein E., Haehnelt M. G., 2017, *MNRAS*, **465**, 3429
- Chardin J., Kulkarni G., Haehnelt M. G., 2018, *MNRAS*, **478**, 1065
- Choudhury T. R., Paranjape A., Bosman S. E. I., 2021, *MNRAS*, **501**, 5782
- Cohen A., Fialkov A., Barkana R., Lotem M., 2017, *MNRAS*, **472**, 1915
- Concerto Collaboration 2020, *A&A*, **642**, A60
- Cothard N. F., et al., 2020, *Journal of Low Temperature Physics*, **199**, 898
- D'Aloisio A., McQuinn M., Trac H., 2015, *ApJ*, **813**, L38
- Davies F. B., Furlanetto S. R., 2016, *MNRAS*, **460**, 1328
- Davies F. B., et al., 2018, *ApJ*, **864**, 142
- DeBoer D. R., et al., 2017, *PASP*, **129**, 045001
- Dillon J. S., Parsons A. R., 2016, *ApJ*, **826**, 181
- Dillon J. S., et al., 2014, *Phys. Rev. D*, **89**, 023002
- Dillon J. S., et al., 2015, *Phys. Rev. D*, **91**, 123011
- Dumitru S., Kulkarni G., Lagache G., Haehnelt M. G., 2019, *MNRAS*, **485**, 3486
- Eilers A.-C., Davies F. B., Hennawi J. F., 2018, *ApJ*, **864**, 53
- Fan X., et al., 2006, *AJ*, **132**, 117
- Fialkov A., Barkana R., Visbal E., 2014, *Nature*, **506**, 197
- Field G. B., 1958, *Proceedings of the IRE*, **46**, 240
- Furlanetto S. R., Oh S. P., Briggs F. H., 2006, *Phys. Rep.*, **433**, 181
- Ghara R., Choudhury T. R., Datta K. K., 2015, *MNRAS*, **447**, 1806
- Ghara R., et al., 2020, *MNRAS*, **493**, 4728
- Ghara R., Giri S. K., Ciardi B., Mellema G., Zaroubi S., 2021, *MNRAS*, **503**, 4551
- Gnedin N. Y., Shaver P. A., 2004, *ApJ*, **608**, 611
- González M., Velarde P., García-Fernández C., 2008, in Pogorelov N. V., Audit E., Zank G. P., eds, *Astronomical Society of*

- the Pacific Conference Series Vol. 385, Numerical Modeling of Space Plasma Flows. p. 91
- Greig B., Mesinger A., Haiman Z., Simcoe R. A., 2017, *MNRAS*, **466**, 4239
- Greig B., Mesinger A., Bañados E., 2019, *MNRAS*, **484**, 5094
- Haardt F., Madau P., 2012, *ApJ*, **746**, 125
- Hutter A., 2018, *MNRAS*, **477**, 1549
- Hutter A., Dayal P., Yepes G., Gottlöber S., Legrand L., Ucci G., 2021, *MNRAS*, **503**, 3698
- Jacobs D. C., et al., 2016, *ApJ*, **825**, 114
- Jensen H., et al., 2013, *MNRAS*, **435**, 460
- Kashino D., Lilly S. J., Shibuya T., Ouchi M., Kashikawa N., 2020, *ApJ*, **888**, 6
- Keating L. C., Puchwein E., Haehnelt M. G., 2018, *MNRAS*, **477**, 5501
- Keating L. C., Weinberger L. H., Kulkarni G., Haehnelt M. G., Chardin J., Aubert D., 2020a, *MNRAS*, **491**, 1736
- Keating L. C., Kulkarni G., Haehnelt M. G., Chardin J., Aubert D., 2020b, *MNRAS*, **497**, 906
- Kimm T., Katz H., Haehnelt M., Rosdahl J., Devriendt J., Slyz A., 2017, *MNRAS*, **466**, 4826
- Kolopanis M., et al., 2019, *ApJ*, **883**, 133
- Koopmans L., et al., 2015, Advancing Astrophysics with the Square Kilometre Array (AASKA14), p. 1
- Kulkarni G., Hennawi J. F., Oñorbe J., Rorai A., Springel V., 2015, *ApJ*, **812**, 30
- Kulkarni G., Keating L. C., Haehnelt M. G., Bosman S. E. I., Puchwein E., Chardin J., Aubert D., 2019a, *Mon. Not. Roy. Astron. Soc.*, **485**, L24
- Kulkarni G., Worseck G., Hennawi J. F., 2019b, *MNRAS*, **488**, 1035
- La Plante P., Battaglia N., Natarajan A., Peterson J. B., Trac H., Cen R., Loeb A., 2014, *ApJ*, **789**, 31
- Levermore C. D., 1984, *J. Quant. Spectrosc. Radiative Transfer*, **31**, 149
- Li W., et al., 2019, *ApJ*, **887**, 141
- Ma Q.-B., Ciardi B., Eide M. B., Busch P., Mao Y., Zhi Q.-J., 2021, *ApJ*, **912**, 143
- Madau P., Fragos T., 2017, *ApJ*, **840**, 39
- Madau P., Meiksin A., Rees M. J., 1997, *ApJ*, **475**, 429
- Majumdar S., Mellema G., Datta K. K., Jensen H., Choudhury T. R., Bharadwaj S., Friedrich M. M., 2014, *MNRAS*, **443**, 2843
- Mao Y., Shapiro P. R., Mellema G., Iliev I. T., Koda J., Ahn K., 2012, *MNRAS*, **422**, 926
- Mason C. A., Treu T., Dijkstra M., Mesinger A., Trenti M., Pentericci L., de Barros S., Vanzella E., 2018, *ApJ*, **856**, 2
- McGreer I., Mesinger A., D'Odorico V., 2015, *Mon. Not. Roy. Astron. Soc.*, **447**, 499
- Mebane R. H., Mirocha J., Furlanetto S. R., 2020, *MNRAS*, **493**, 1217
- Mertens F. G., et al., 2020, *MNRAS*, **493**, 1662
- Mesinger A., Furlanetto S., Cen R., 2011, *MNRAS*, **411**, 955
- Mesinger A., Ewall-Wice A., Hewitt J., 2014, *MNRAS*, **439**, 3262
- Mirocha J., Furlanetto S. R., Sun G., 2017, *MNRAS*, **464**, 1365
- Morgan S., Jacobs D., Beardsley A., 2019, in American Astronomical Society Meeting Abstracts #233. p. 349.22
- Nasir F., D'Aloisio A., 2020, *MNRAS*, **494**, 3080
- Oñorbe J., Hennawi J. F., Lukić Z., 2017, *ApJ*, **837**, 106
- Paciga G., et al., 2013, *MNRAS*, **433**, 639
- Park J., Gillet N., Mesinger A., Greig B., 2020, *MNRAS*, **491**, 3891
- Parsons A. R., et al., 2010, *AJ*, **139**, 1468
- Parsons A., Pober J., McQuinn M., Jacobs D., Aguirre J., 2012, *ApJ*, **753**, 81
- Patil A. H., et al., 2017, *ApJ*, **838**, 65
- Patwa A. K., Sethi S., Dwarakanath K. S., 2021, *MNRAS*, **504**, 2062
- Paul S., et al., 2016, *ApJ*, **833**, 213
- Pawlik A. H., Schaye J., van Scherpenzeel E., 2009, *MNRAS*, **394**, 1812
- Planck Collaboration 2016, *A&A*, **594**, A13
- Planck Collaboration 2020, *A&A*, **641**, A6
- Planck Collaboration XVI 2014, *A&A*, **571**, A16
- Pober J. C., et al., 2013, *AJ*, **145**, 65
- Pober J. C., et al., 2014, *ApJ*, **782**, 66
- Pritchard J. R., Loeb A., 2012, *Reports on Progress in Physics*, **75**, 086901
- Qin Y., Mesinger A., Bosman S. E. I., Viel M., 2021, arXiv e-prints, p. arXiv:2101.09033
- Raste J., Sethi S., 2018, *ApJ*, **860**, 55
- Raste J., Sethi S., 2019, *ApJ*, **876**, 56
- Santos M. G., Ferramacho L., Silva M. B., Amblard A., Cooray A., 2010, *MNRAS*, **406**, 2421
- Sethi S. K., 2005, *MNRAS*, **363**, 818
- Shaver P. A., Windhorst R. A., Madau P., de Bruyn A. G., 1999, *A&A*, **345**, 380
- Springel V., 2005, *MNRAS*, **364**, 1105
- Springel V., Yoshida N., White S. D. M., 2001, *New Astron.*, **6**, 79
- Thompson A. R., Moran J. M., Swenson George W. J., 2001, Interferometry and Synthesis in Radio Astronomy, 2nd Edition
- Tingay S. J., et al., 2013, *Publ. Astron. Soc. Australia*, **30**, e007
- Trenti M., Stiavelli M., Bouwens R. J., Oesch P., Shull J. M., Illingworth G. D., Bradley L. D., Carollo C. M., 2010, *ApJ*, **714**, L202
- Trott C. M., et al., 2020, *MNRAS*, **493**, 4711
- Venkatesan A., Giroux M. L., Shull J. M., 2001, *ApJ*, **563**, 1
- Viel M., Haehnelt M. G., Springel V., 2004, *MNRAS*, **354**, 684
- Wang F., et al., 2020, *ApJ*, **896**, 23
- Wayth R. B., et al., 2018, *Publ. Astron. Soc. Australia*, **35**, 33
- Weinberger L. H., Haehnelt M. G., Kulkarni G., 2019, *MNRAS*, **485**, 1350
- Weinberger L. H., Kulkarni G., Haehnelt M. G., 2020, *MNRAS*, **494**, 703
- Wouthuysen S. A., 1952, *AJ*, **57**, 31
- Yatawatta S., et al., 2013, *A&A*, **550**, A136
- Zahn O., Mesinger A., McQuinn M., Trac H., Cen R., Hernquist L. E., 2011, *MNRAS*, **414**, 727
- de Lera Acedo E., et al., 2020, SKA LFAA Station Design Report (arXiv:2003.12744)
- van Haarlem M. P., et al., 2013, *A&A*, **556**, A2

APPENDIX A: 21-CM POWER SPECTRUM UPPER LIMITS

In Figure 6, we have compared the 21-cm brightness temperature power spectrum from our model with a model of early reionization at $k = 0.08 h/cMpc$, $0.2 h/cMpc$ and $0.5 h/cMpc$. We also compare these model predictions with a compilation of 21-cm power spectrum upper limits reported by GMRT (Paciga et al. 2013), LOFAR (Patil et al. 2017; Mertens et al. 2020), MWA (Dillon et al. 2014, 2015; Beardsley et al. 2016; Paul et al. 2016; Barry et al. 2019; Li et al. 2019; Trott et al. 2020; Patwa et al. 2021) and PAPER (Kolopanis et al. 2019). The numerical values of these limits are listed in Table A1.

This paper has been typeset from a $\text{\TeX}/\text{\LaTeX}$ file prepared by the author.

Table A1. A compilation of the 21-cm power spectrum upper limits reported by GMRT, LOFAR, MWA and PAPER at redshifts $5 \leq z \leq 10$ at k -modes close to 0.08 $h/c\text{Mpc}$, 0.2 $h/c\text{Mpc}$ and 0.5 $h/c\text{Mpc}$. Figure 6 compares these values with our predictions.

z	k [$h/c\text{Mpc}$]	$\Delta_{21}(k)$ [mK]
GMRT: Paciga et al. (2013)		
8.6	0.10	443
8.6	0.19	1156
8.6	0.50	248
LOFAR: Patil et al. (2017)		
7.9–8.6	0.083	220.9
7.9–8.6	0.128	407.7
8.6–9.6	0.083	184.7
8.6–9.6	0.128	342.0
9.6–10.6	0.083	148.6
9.6–10.6	0.128	366.1
LOFAR: Mertens et al. (2020)		
9.1	0.075	72.86
9.1	0.179	246.92
9.1	0.432	683.20
MWA: Dillon et al. (2014)		
6.2	0.093	8.25×10^3
6.2	0.246	1.59×10^4
6.2	0.487	3.69×10^4
6.5	0.081	6.88×10^3
6.5	0.233	9.89×10^3
6.5	0.457	2.09×10^4
6.8	0.084	8.63×10^3
6.8	0.233	1.06×10^4
6.8	0.451	2.40×10^4
7.2	0.080	1.03×10^4
7.2	0.225	1.36×10^4
7.2	0.446	2.87×10^4
7.6	0.074	2.31×10^3
7.6	0.233	4.47×10^3
7.6	0.426	8.83×10^3
8.0	0.073	1.10×10^3
8.0	0.214	2.79×10^3
8.0	0.424	4.61×10^3
8.4	0.070	5.40×10^2
8.4	0.206	3.06×10^3
8.4	0.419	5.66×10^3
9.0	0.069	3.50×10^2
9.0	0.200	3.93×10^3
9.0	0.405	7.27×10^3
9.5	0.067	3.00×10^2
9.5	0.197	1.80×10^3
9.5	0.399	3.18×10^3
MWA: Dillon et al. (2015)		
6.2–6.6	0.181	1.93×10^2
6.2–6.6	0.537	7.87×10^2
6.6–7.0	0.176	1.90×10^2
6.6–7.0	0.526	9.17×10^2
7.0–7.5	0.195	2.74×10^2
7.0–7.5	0.550	1.02×10^3

Table A1 – *continued* 21-cm power spectrum upper limits

z	k [$h/c\text{Mpc}$]	$\Delta_{21}(k)$ [mK]
MWA: Beardsley et al. (2016)		
6.5	0.20	193.80
6.5	0.53	259.29
6.8	0.20	213.57
6.8	0.52	284.80
7.1	0.20	215.44
7.1	0.51	263.30
MWA: Paul et al. (2016)		
8.2	0.184	295.3
8.2	0.462	1175.6
MWA: Barry et al. (2019)		
7.0	0.200	62.37
7.0	0.523	266.27
MWA: Li et al. (2019)		
6.5	0.222	102.96
6.5	0.554	93.59
6.8	0.217	97.01
6.8	0.542	164.62
7.1	0.212	109.09
7.1	0.531	157.48
MWA: Trott et al. (2020)		
6.5	0.212	70.20
6.5	0.495	125.50
6.8	0.212	90.00
6.8	0.495	169.00
7.1	0.212	117.40
7.1	0.495	231.90
7.8	0.212	247.50
7.8	0.495	466.80
8.2	0.212	376.30
8.2	0.495	1402.60
8.7	0.212	544.70
8.7	0.495	1341.00
MWA: Patwa et al. (2021)		
8.2	0.20	1000
PAPER: Kolopanis et al. (2019)		
7.48	0.069	1.46×10^5
7.48	0.231	1454.36
7.48	0.506	1044.32
8.13	0.066	1.59×10^5
8.13	0.223	1543.91
8.13	0.488	446.38
8.37	0.065	1.50×10^5
8.37	0.220	1421.33
8.37	0.534	329.58
8.68	0.064	1.50×10^5
8.68	0.217	1232.40
8.68	0.525	386.66
9.93	0.060	2.21×10^5
9.93	0.204	2231.54
9.93	0.495	4564.18